Residual stresses and porosity in Ti-6Al-4V produced by laser powder bed fusion as a function of process atmosphere and component design

Additive Manufacturing 47 (2021) 102340

Contents lists available at ScienceDirect

Additive Manufacturing

journal homepage: www.elsevier.com/locate/addma

Research Paper

Residual stresses and porosity in Ti-6Al-4V produced by laser powder bed fusion as a function of process atmosphere and component design

C. Pauzon [a,*], T. Mishurova [b], S. Evsevleev [b], S. Dubiez-Le Goff [c], S. Murugesan [c], G. Bruno [b,d], E. Hryha [a]

[a] Chalmers University of Technology, Industrial and Materials Science, Rännvägen 2A, Göteborg 41296, Sweden
[b] Bundesanstalt für Materialforschung und–prüfung (BAM), Unter den Eichen 87, Berlin 12205, Germany
[c] Linde GmbH, Linde Technology – Global Development, Carl-von-Linde-Straße 25, Unterschleißheim 85716, Germany
[d] Institute of Physics and Astronomy, University of Potsdam, Karl-Liebknecht-Straße 24–25, Potsdam 14476, Germany

ARTICLE INFO

Keywords:
Residual stresses
Laser powder bed fusion
Process atmosphere
Helium
Ti-6Al-4V

ABSTRACT

The influence of the process gas, laser scan speed, and sample thickness on the build-up of residual stresses and porosity in Ti-6Al-4V produced by laser powder bed fusion was studied. Pure argon and helium, as well as a mixture of those (30% helium), were employed to establish process atmospheres with a low residual oxygen content of 100 ppm O_2. The results highlight that the subsurface residual stresses measured by X-ray diffraction were significantly lower in the thin samples (220 MPa) than in the cuboid samples (645 MPa). This difference was attributed to the shorter laser vector length, resulting in heat accumulation and thus in-situ stress relief. The addition of helium to the process gas did not introduce additional subsurface residual stresses in the simple geometries, even for the increased scanning speed. Finally, larger deflection was found in the cantilever built under helium (after removal from the baseplate), than in those produced under argon and an argon-helium mixture. This result demonstrates that complex designs involving large scanned areas could be subjected to higher residual stress when manufactured under helium due to the gas's high thermal conductivity, heat capacity, and thermal diffusivity.

1. Introduction

Metal additive manufacturing (AM) and, in particular, laser powder bed fusion (L-PBF) have disrupted traditional manufacturing routes and created almost unlimited possibilities for designers to revise components' geometries and assemblies to improve component functionality and hence maximize benefits from this technology. L-PBF uses the energy from a laser to locally melt and solidify a bed of metallic powder in a layer-wise fashion. This approach allows the production of near-net-shape complex parts with thin features and integrated functionality. With the development of L-PBF hardware and L-PBF processing, the most used alloys, such as 316L stainless steel, Alloy 718, and Ti-6Al-4V can be produced to full density with strength comparable to or higher than conventionally produced materials [1]. However, several challenges remain for L-PBF adoption in industrial production schemes. Increased productivity, process, and quality control are key aspects of such challenges.

The high heating and cooling rates in the L-PBF process, and thus significant temperature gradient around the melt pool, are responsible for the appearance of high internal stresses [2]. The latter can lead to significant component distortion when released and, occasionally, process failure as the powder recoater collides with the warped top surface of the part. Therefore, internal stress is a threat to both dimensional accuracy and productivity. Moreover, internal stress leads to residual stress, which can be deleterious for both mechanical properties and operational life. Residual stresses are usually relieved by post heat treatments on the components while they are still attached to the baseplate. Among many others, the recent work by Mishurova et al. [3] revealed that laser parameters can be tuned to control the subsurface residual stresses in Ti-6Al-4V. Residual stresses were proven to decrease for higher energy inputs (i.e., lower laser scanning speed or hatch distance). In fact, the optimization of laser parameters remains the favoured approach for medium-sized installations [4], as well as for the development of high-strength, low-volume structures such as lattices [5]. Although reducing the scanning speed can be detrimental to productivity, the development of larger hardware with multi-lasers and

* Corresponding author.
E-mail address: pauzon@chalmers.se (C. Pauzon).

https://doi.org/10.1016/j.addma.2021.102340
Received 24 January 2021; Received in revised form 9 June 2021; Accepted 15 September 2021
Available online 20 September 2021

high-power laser systems is promising for increased process productivity [6].

Among the commonly optimized process variables, the first order parameters are usually connected to the laser scanning speed, power, and scanning strategy. Recent work has highlighted that the process atmosphere also affects the process stability in terms of residual gas impurities [7] and gas type [8]. Processing under helium-rich atmosphere has been proven to reduce the generation of spatters by Pauzon et al. [9] with Ti-6Al-4V and by Traore et al. [10] with Inconel® 625. This reduction was attributed to a faster expansion of the vapour generated at the melt pool, which results in a limited heat accumulation in the vicinity of the melt pool, commonly responsible for excessive instabilities leading to melt pool ejections. Researchers have, therefore, proposed that the addition of helium can be beneficial to further increase the productivity of the L-PBF process. In further recent work, we demonstrated that helium can also be used to process 316L stainless steel at high build rates (37% increase) without compromising its tensile properties [11]. As explained by Mishurova et al. [3], an optimization of process parameters toward a productivity increase may be connected to an increase in residual stresses and porosity. Thus, assessing the effect of helium addition to the process atmosphere on the increasing build rate for Ti-6Al-4V is critical.

In the present work, the use of pure helium and a mixture of helium (30%) and argon was compared to that of pure argon to produce Ti-6Al-4V samples by L-PBF. An increase in productivity was investigated by considering different laser scanning speeds. In addition, the effect of sample thickness was studied to establish the possible effect of processing gas on heat accumulation, and hence, on residual stresses and porosity. The produced material was analysed to determine its chemistry, porosity in the as-built state, and residual stresses. A combination of accurate residual oxygen monitoring and high-resolution analytical tools from scanning electron microscopy to X-ray computed tomography and X-ray diffraction enabled in-depth insights into the L-PBF process parameters/material properties relationship.

2. Materials and methods

2.1. Samples production

The material studied in this work was produced on an EOS M290 (EOS GmbH) machine equipped with a Yb-fibre laser with 400 W nominal maximum power, using gas atomized Ti-6Al-4V powder with particles size in the range of 15–45 μm. Samples were produced with cuboid ($5 \times 5 \times 15$ mm^3) and plate ($1 \times 5 \times 15$ mm^3) geometries directly on the baseplate to investigate the effect of sample thickness on residual stresses (see Fig. 1). Two sets of laser parameters were employed to produce both geometries with the three gases (12 sample types): the standard laser parameters developed by the machine manufacturer under the license *Ti64_PerformanceM291 1.10* (details are the property of the manufacturer) and a custom set with increased scanning speed. These parameters are called standard (Std) and high speed (HS) in the following text. The two sets use a 30 μm layer thickness to build the samples. The licensed laser parameter set was extensively optimized and consisted of a sequence of in-fill (inside the area to be scanned), contour scanning, and up-skin exposures (for the last top layers). The in-fill scan vector pattern is rotated by 67° between each deposited layer. This is the strategy typically preferred for the mitigation of residual stresses. The custom parameter set was defined to be identical to the standard set, except for an increased in-fill scanning speed (by 500 mm/s or a 40% increase), resulting in a volumetric energy density decrease of about 30%. Three samples for each combination of geometry and parameter set were produced simultaneously on one baseplate. The defined build job was repeated using high purity argon, helium, and a mixture of the two with 30% helium (VarigonHe30) as process gases. Both Argon 5.0 and Helium 5.0 had less than 10 ppm of impurities (such as O_2), while VarigonHe30 had less than 40 ppm of impurities. An external oxygen monitoring system, the ADDvanceO2® precision (Linde AG), was connected to the L-PBF machine to monitor the residual oxygen level in the process atmosphere prior to and during printing around 100 ppm O_2. This step ensured no side-effects (e.g., oxygen and nitrogen pick-up, embrittlement) connected to the residual impurities. These impurities' detrimental effect on the properties of Ti-6Al-4V produced by L-PBF has been demonstrated by several authors [7, 12]. Finally, after production, the samples were removed from the baseplate using a bandsaw and then studied in their as-built condition.

To further study the relaxation of residual stresses in large L-PBF components, additional cantilever structures were printed. These structures were produced using the same powder feedstock and the standard laser parameters set under argon, helium, and their mixture (always maintaining a maximum of 100 ppm residual O_2).

2.2. Subsurface residual stresses

Subsurface residual stress analysis was conducted on the laboratory energy dispersive diffractometer LIMAX-160 at Helmholtz Zentrum Berlin, Germany. The basis for the generation of X-rays on this diffractometer is a MetalJet source from Excillum (Model D2), featuring a liquid Ga-rich alloy as anode material. Since the anode flows continuously, it is possible to work with a high electron density even at high acceleration voltages and, in this way, generate a source with a small size and a significantly higher photon flux compared to conventional X-ray tubes. The LIMAX-160 instrument allows acceleration voltages up to 160 kV. A polycapillary primary optic with a circular collimator (ø 0.5 mm) was used. Residual stress on the surface of cuboid and plate samples was determined using the $sin^2\psi$ method (where ψ is the tilt angle around the X axis) in reflection mode with a diffraction angle of

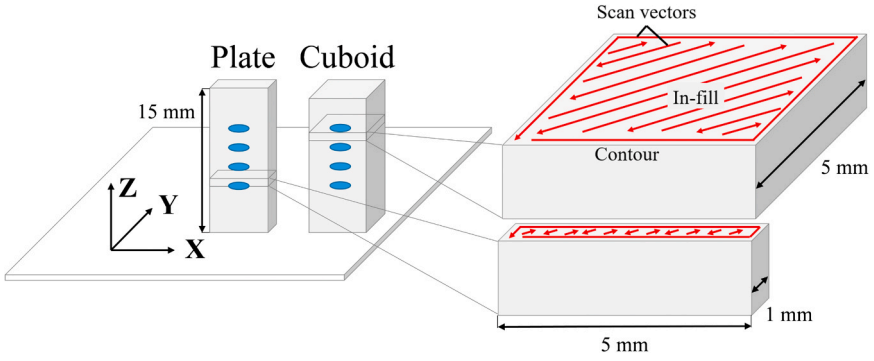

Fig. 1. Schemes of the two printed geometries and close-up of a single layer where the laser scanning pattern is displayed. The in-fill and contour scanning are distinguished. The blue ellipses represent the sites were subsurface residual stresses were measured. (For interpretation of the references to colour in this figure legend, the reader is referred to the web version of this article.)

16° (see both [13,14] for further details about the experiment geometry). A few points along the building direction were measured on the samples' lateral surface (schematically displayed as blue ellipses in Fig. 1). Assuming the normal component to the surface is zero, the residual stress component along the building direction (axis Z; see Fig. 1) was determined.

The energy dispersive diffraction (EDD) technique allows probing different depths (from the surface), thus overcoming the issue of high surface roughness often present in L-PBF parts [15]. The application of EDD for residual stress mapping of L-PBF manufactured samples are reported elsewhere [14,16,17]. The {103} α-Ti crystallographic plane, corresponding to a characteristic depth of around 45 μm from the surface, was used for the analysis (the characteristic depth is defined as the one where only $1/e$ of the intensity is available). The EDDIDAT (Energy-Dispersive Diffraction Data Analysis Tool) software was used for diffraction peak fitting and residual stress calculation [18]. The X-ray diffraction elastic constants (DEC) were calculated with the Eshelby-Kröner model: $s_1 = -2.579 \times 10^{-6}$ MPa^{-1} and $\frac{1}{2}s_2 = 10.870 \times 10^{-6}$ MPa^{-1} [19].

2.3. Cantilever structures

The component's distortions induced by the relaxation of residual stress after removal from the baseplate are a bottleneck for the warranty of dimension tolerances. Considerable effort has been made to understand the distortion occurring in L-PBF produced parts and in the development of predictive models [20]. A popular approach to calibrate and verify such numerical models is printing specific designs and measuring their distortions [21]. Cantilevers are structures featuring a long overhanging surface supported by several, usually equally spaced, supporting blocks. During L-PBF, the distortion of the overhanging volume is limited by the supporting structure. After production, when the supports are cut, the cantilever deforms to accommodate the redistribution of stresses within the new geometry. Therefore, the measurement of the cantilever's deflection provides an estimation of the relaxation of residual stresses locked after the L-PBF process. This approach was followed to further investigate the effect of the process gas. The produced cantilevers were 100 mm long and featured 20 supporting blocks of 2 mm thickness, evenly spaced by 2 mm (see Fig. 2). After printing, these blocks were cut using a bandsaw at a 2 mm distance from the baseplate. A procedure was developed to ensure consistent parallelism between the bandsaw and the baseplate. The deflections were measured using a digital caliper.

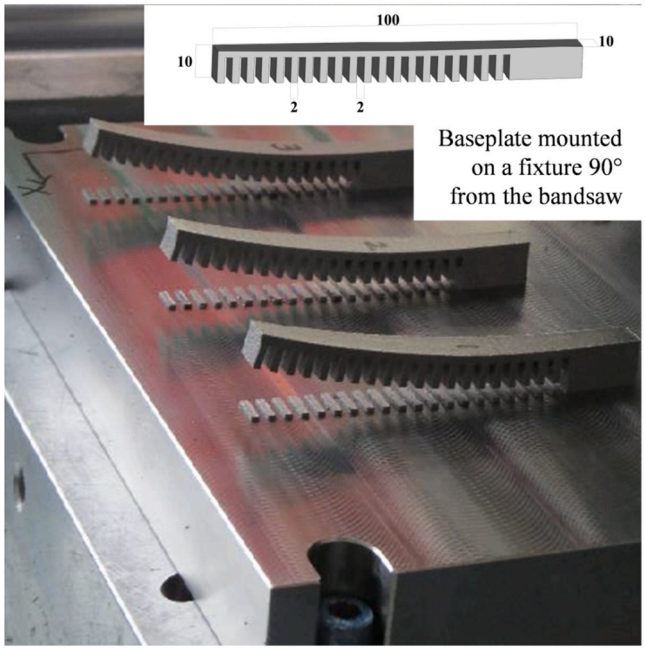

Fig. 2. Photograph of the cantilever structures after being cut from the baseplate. The insert illustrates the geometry of the cantilever structures.

2.4. X-ray computed tomography

Laboratory X-ray computed tomography (XCT) for porosity analysis was performed by using a v|tome|x L 300 CT scanner from General Electric. With an acquisition time of 2 s for each projection, 2500 projections were acquired during each scan. A tube voltage of 125 kV, a current of 70 μA, and a voxel size of $(8\ \mu m)^3$ were used. Data processing and visualization were performed by using Fiji ImageJ [22] and AvizoFire 9.4 software [23]. Only voids with a minimum volume of 10 voxels were considered to reduce the probability of false segmentation. Thus, pores with minimum equivalent diameter of around 20 μm were detected. To account for errors in segmentation, three different threshold values were taken, and the standard deviation among the determined volume fractions was calculated. For the calculation of the porosity volume fraction distribution from the lateral surface to the centre, the Euclidean distance transformation was applied. The distance transform generates a map, in which, for every point in the sample, the corresponding shortest distance to the nearest edge is calculated.

Synchrotron XCT (SXCT) was conducted at the BAMline, BESSY II (Berlin, Germany), which is presented in details in [24]. For the measurements, sister samples were machined to the cylindrical shape with a diameter of 1 mm. The energy of the monochromatic X-ray beam was set to 45 keV, and an effective pixel size of 0.88 μm was achieved using a CCD camera with 10 × objective and binning 2 × 2 pixels into one; 2500 projections were acquired, each with a counting time of 1.7 s. The reconstruction of 3D volumes from 2D projections was made by BAM in-house developed filtered back projection software and a single-distance phase-contrast correction algorithm [25], using ANKAphase software [26].

2.5. Microstructure, hardness, and chemical composition

One sample of each geometry and parameter set was mounted in conductive resin to analyse the microstructure along the building direction. Then, these samples were ground down at least 200 μm to observe bulk features. The samples were finally polished until a final step using a MD-Chem cloth (Struers) and a mixture of OP-S (colloidal suspension) with H_2O_2 for 15 min. The microstructures were revealed by chemical etching using Kroll's reagent (100 mL H_20, 3 mL HF, and 6 mL HNO_3) and high-resolution scanning electron microscopy (SEM) with a LEO Gemini 1550 instrument (Zeiss). These samples were also studied by light optical microscopy using a Axioscope 7 (Zeiss). The Vickers hardness (HV1) was measured on standard samples' polished cross-sections with a DuraScan system (Struers). The results displayed below are the average of at least 10 measurements spaced by at least three indentation dimensions. The oxygen and nitrogen contents were measured in the produced samples by carrier hot gas extraction using a LECO ONH836 system. The reported results are the average of at least three measurements.

Finally, electron backscattered diffraction (EBSD) analyses were performed on the polished cross-sections of plate and cuboid samples parallel to the XY plane in Fig. 1, so perpendicular to the building direction Z, with a Zeiss Gemini 450 SEM. A 1.5 μm step size and 500 × magnification were employed to acquire EBSD maps over the XY cross-sections, of dimensions $3 \times 1.2\ mm^2$ for the cuboids and $3 \times 0.8\ mm^2$ for the plates. The obtained data were post-processed using HKL-Channel 5™. Based on the Burger Orientation Relationship (BOR) existing between the body-centered cubic β phase and the hexagonal α phase, the parent β grains were numerically reconstructed using the MATLAB toolbox MTex.

3. Results

3.1. Chemistry and hardness

Table 1 lists the oxygen and nitrogen contents in the cuboids produced using the standard laser parameters and the three studied process gases. The oxygen is slightly lower and the nitrogen higher in the Ti-6Al-4V cuboid produced in helium than in the other gases. For argon and VarigonHe30, a slight increase of oxygen content for the cuboids compared to the powder is present. Finally, regardless of the process atmosphere, not all the nitrogen from the feedstock powder was transferred to the built material during L-PBF, which should be investigated in future studies. Overall, the noted chemistry differences between the samples are relatively minor, which is reflected in the similar hardness values.

3.2. Microstructure, density, and defects

All the produced samples exhibit the typical microstructure of Ti-6Al-4V produced by L-PBF. This microstructure consists of a fine and hierarchical martensitic structure, as apparent in the high magnification SEM micrographs taken at different positions for a cuboid sample printed under argon atmosphere (see Fig. 3). Only images of this sample are displayed as others are similar and it is the reference atmosphere for all L-PBF systems. The hierarchical aspect of the microstructure was explained by Yang et al. [27]; they associated it with repeated heating of the previously deposited layer into the high temperature β-phase field. They explained that thick primary α/α' lamellae form during the first cooling cycle, while thinner secondary and then tertiary lamellae form during the subsequent fast cooling cycles. In addition, a band-like contrast was also revealed upon etching of the cross-section along the building direction. The microstructure appears to exhibit many successive bands with spacing about 100 μm. Such band contrast has been reported for Ti-6Al-4V built by AM. For example, Liu and Shin [28] highlighted the presence of layer bands in Ti-6Al-4V produced both by directed energy deposited and by L-PBF. These bands are formed by the local coarsening of the reheated layers' microstructure. Overall, the microstructure seems homogeneous along the height of the samples and close to the part's edge. Similar features were observed in all samples, regardless of the tested atmospheres, sample design, and in-fill scanning speeds and despite differences in the porosity levels reported below.

The porosity volume fraction obtained by laboratory XCT is summarized in Table 2. The error in segmentation was around ± 0.005% for standard parameter samples and around ± 0.03% for high-speed parameter samples. Samples produced under a helium atmosphere had a consistently larger volume fraction of pores compared with VarigonHe30 or argon. The increased scanning speed led to an increase in the porosity from approximately 0.01–0.2%. The sample geometry did not have a large impact on the porosity as it was similar for cuboid and plate samples.

The porosity spatial distributions projected onto the build plane (XY plane; see Fig. 1) for cuboid samples are provided in Fig. 4. Such distributions display an increase of the porosity for high-speed cuboids compared to standard ones. Furthermore, the concentration of pores near the surface of the samples was clearly observed for HS samples (Fig. 4d, e, and f) and is also slightly visible for Std samples (Fig. 4a, b, and c). The porosity formation in the subsurface region, when the contour scan is applied, has often been reported in [29,30] for Ti-6Al-4V cubes and more complex designs, and in [14] for Ti-6Al-4V cubes, with the exception of cubes built with low scanning speed (200 mm/s). In addition, it seems that a region of higher density (i.e., pore depletion) was observed on the right side of the HS samples. This result could be due to the orientation of the samples with respect to the gas flow.

Table 1
Hardness (HV1) measured for the cuboids, and oxygen and nitrogen contents measured in the powder and cuboid samples produced using the standard laser parameters and argon, VarigonHe30, and helium as process gases.

Process atmosphere	O [ppm]	N [ppm]	HV1
Ti-6Al-4 V powder	1692 ± 27	166 ± 10	N. A.
Argon Cuboid Std	1735 ± 97	92 ± 23	409 ± 23
VarigonHe30 Cuboid Std	1781 ± 188	62 ± 20	415 ± 13
Helium Cuboid Std	1690 ± 213	123 ± 27	414 ± 13

Table 2
The porosity volume fraction obtained by XCT.

Sample	Argon	VarigonHe30	Helium
Plate HS	0.18%	0.18%	0.27%
Plate Std	0.012%	0.014%	0.016%
Cuboid HS	0.18%	0.19%	0.25%
Cuboid Std	0.0094%	0.0098%	0.0116%

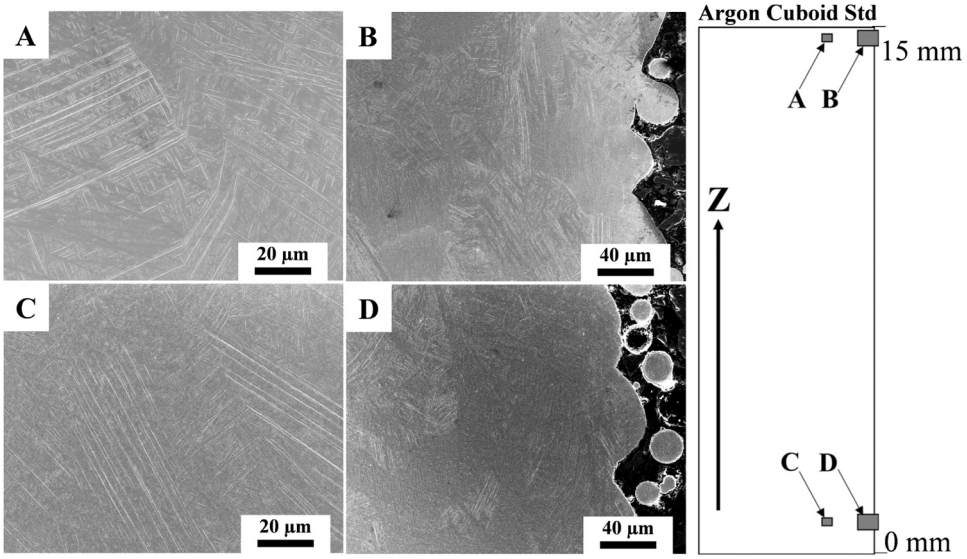

Fig. 3. SEM micrographs of the etched microstructure observed along the building direction Z for the argon cuboid build with standard laser parameters at the top and bottom and close to the surface.

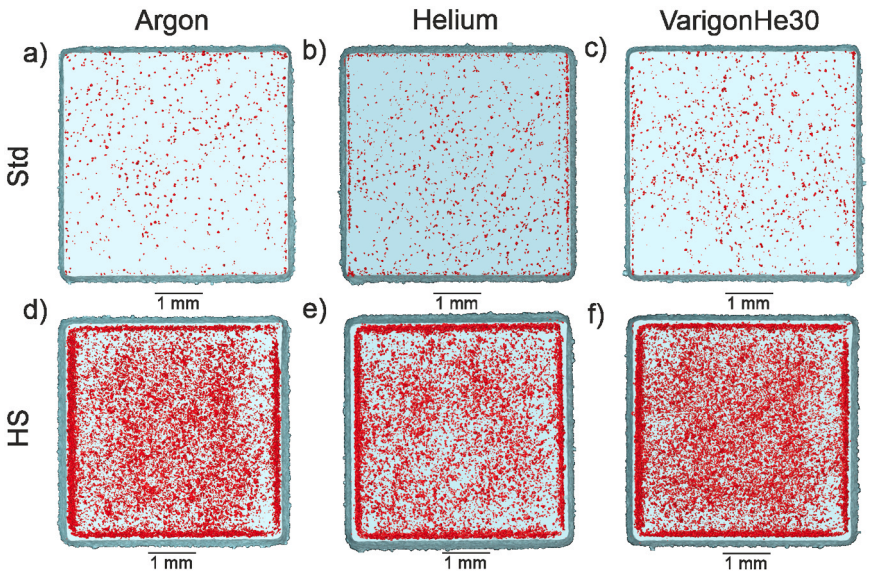

Fig. 4. Porosity projected onto XY plane for cuboids produced with standard speed using (a) argon, (b) helium, (c) VarigonHe30; and cuboids produced with high-speed using (d) argon, (e) helium, and (f) VarigonHe30.

Unfortunately not noted, the higher density side is assumed to lie closer to the gas inlet.

The Euclidean distance transformation allows obtaining the local porosity volume fraction at each distance from the lateral surface (see Fig. 5, solid curves). The local volume fraction was calculated as a ratio of porosity volume at a certain distance to the sample volume contained within this distance. In addition, the total porosity (cumulative volume fraction) was calculated as a function of distance from the lateral surface. The spatial distribution of the porosity volume fraction from the lateral surfaces to the centre of the cuboids (Fig. 5, dashed curves) indicates that the concentration of the pores in the subsurface region was present in every sample. Interestingly, although contour scan parameters were the same, the position of the maximum porosity volume fraction under the surface was different: around 140 μm for HS and 75 μm for Std samples.

In general, the observed pores in the samples produced with high speed exhibited an irregular morphology, typical for lack-of-fusion defects. Fig. 6a displays an example of such defects, and partially melted powder particles are distinguishable. Since SXCT allows for higher resolution than lab XCT (Fig. 4), the shape of the pores can be better distinguished also allowing enhanced statistics compared to the SEM micrographs (Fig. 6b). Indeed, most of the pores in the HS samples were lack-of-fusion defects containing partially molten powder particles, as visible on the magnified view of some defects (Fig. 6b). These pores are correlated to a poor overlap between hatch vectors for increased laser speed and are further explained in the discussion section.

3.3. Subsurface residual stresses

Fig. 7 summarizes the results of the subsurface residual stress analysis for the plate and cuboid samples. For the samples with the same geometry, no systematic difference in residual stress states between the HS and Std samples was present. Furthermore, no effect of the process atmosphere on the subsurface residual stress was detected. However, the samples' geometry had an impact on the residual stress: cuboid and plate samples had different stress levels. For the cuboid samples, residual stress varied from 450 MPa to 800 MPa with a mean value of 645 MPa, and for the plate samples, residual stress ranged from 50 MPa to 400 MPa with a mean value of 220 MPa.

3.4. Deformation of cantilever structures

Fig. 8 displays the deflection along the cantilever structures after the supporting blocks were cut. Regardless of the process atmosphere, all structures bent significantly upward, highlighting the release of strong residual stresses present in the as-built condition in the upper part of the cantilevers. This phenomenon was observed and explained by Li et al. [31] and is elaborated on in the discussion section. The deflection appears to be 1.4 mm greater for the cantilever produced under helium than for that produced under argon, which exhibited a maximum deflection of 8.8 mm. The structure built under VarigonHe30 resulted in deflection similar to that obtained under argon. These results suggest that helium's addition in the process atmosphere may increase residual stresses obtained for specific components' design. Stoney [32] developed an equation relating the tension in thin deposited metallic films to the deflection of the substrate. It describes the proportionality of these two by a coefficient dependent on the Young's modulus, the thickness of the film and of the substrate, as well as its length. This equation has already been applied to the deflection of printed metallic components [33], however it appears difficult to define several of the variables such as thickness of the deposited film, and apply it to the cantilever design, which is not a simple beam geometry. Still, one can consider that the proportionality coefficient remains the same between the pure argon and helium case, based on the microstructural investigations. As a result, a 10% increase in deflection distances in helium compared to argon can be connected to an approximate increase of 10% of the residual stresses, estimated to be about 1000 MPa.

4. Discussion

4.1. Porosity variations

The most important drawback of the scanning speed increase is the increase in porosity volume fraction, from 0.016% for standard speed to 0.27% for the high speed in the plate sample produced in helium (see Table 2). Overall, the porosity volume fraction of the samples produced in helium, measured by laboratory XCT, was about 0.1% higher than that of the argon and VarigonHe30 counterparts for both scanning speeds but was more critical for the high-speed samples (see Table 2). For the standard parameter set, the porosity obtained with helium appears to be mostly located close to the part's edge (see Fig. 4b and e).

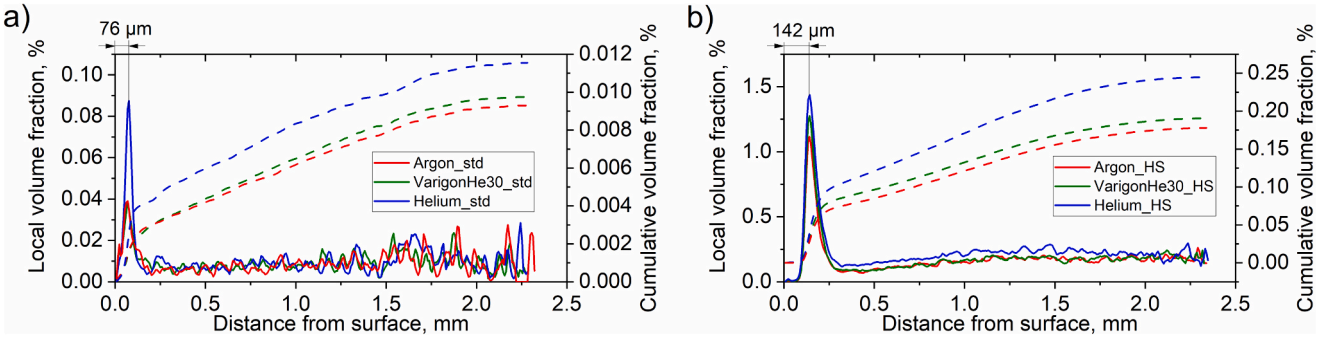

Fig. 5. The volume fraction (solid lines) and cumulative volume fraction (dashed lines) of pores as a function of distance from the lateral surface of cuboids for (a) standard speed and, (b) high speed.

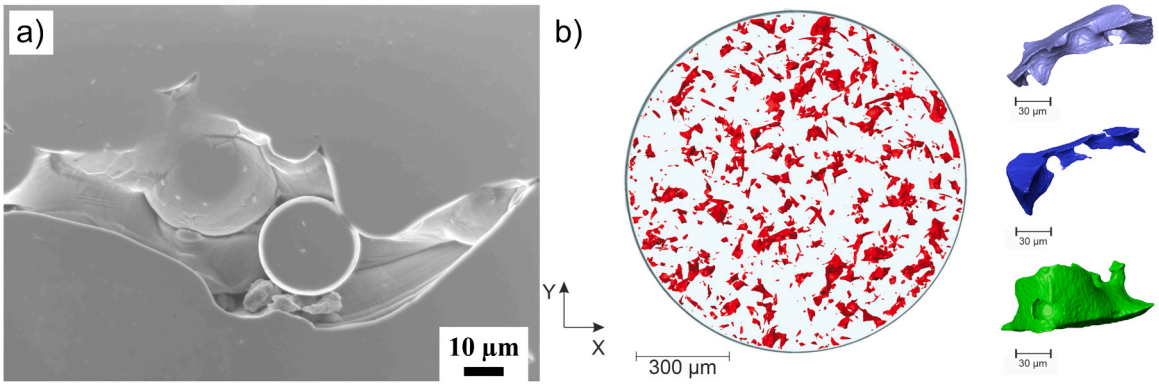

Fig. 6. (a) SEM micrograph of a typical irregular lack-of-fusion defect observed on the cross-section of a cuboid built under argon using a high scan speed and, (b) porosity projected onto the XY plane and 3D rendering of a few pores (obtained from a SXCT reconstruction) for HS sample produced using VarigonHe30.

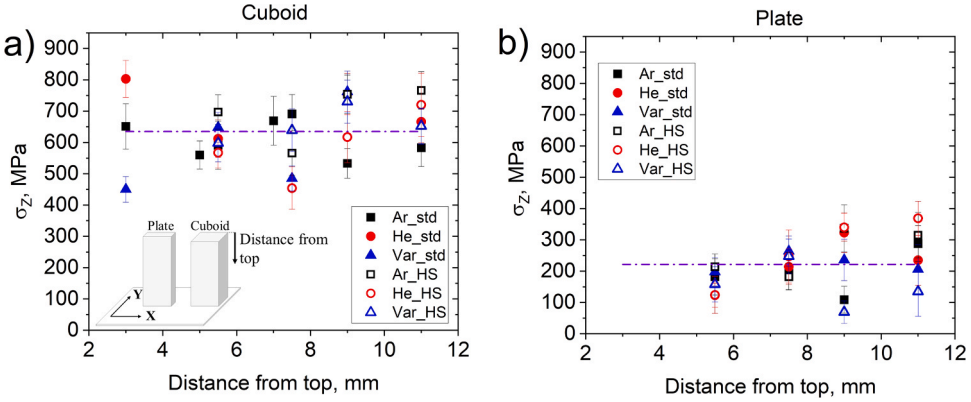

Fig. 7. Residual stresses along the building direction Z as a function of distance from the top of (a) the cuboid samples and, (b) the plate samples. The mean residual stress value of all samples is indicated by a violet dashed line.

This may be connected to denudation which describes the depletion of powder around the melting tracks, and is caused by the entrainment of these particles toward the vapor flow generated above the melt pool. It is mostly critical at the edges of the part but can also lead to a lack of powder particles within the in-fill region and thus to lack-of-fusion defects, as suggested by the cumulative porosity fraction of the helium-produced sample displayed in Fig. 5. As explained by Bidare et al. [34], the denudation could be favoured under helium because of the faster expansion of the vapours in the lower density gas. Still, it should be emphasized that the bulk density achieved with helium is comparable to that obtained with the other gases. Finally, the use of the argon-helium mixture leads, instead, to a porosity distribution resembling that of the samples produced with argon.

The pronounced subsurface porosity observed for all the samples is associated with the poor overlap of the in-fill and contour scanning, as depicted in Fig. 10a for the standard parameter set and evident in Fig. 9. This subsurface porosity was maximum at a distance of 76 µm for the standard parameters (up to 35% of the total porosity) and 142 µm for the high speed (up to 27% of the total porosity), see Fig. 5. In addition, the width of the area where subsurface porosity was observed appears larger for the high-speed samples. Despite the different in-fill scanning speed, the hatch distance and contour parameters were not changed. Therefore, only the melt pool (and thus the melt track) in the in-fill region was narrower for the high-speed samples, resulting in a reduced overlap of

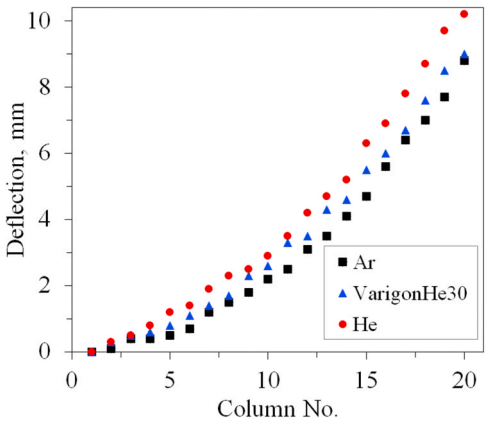

Fig. 8. Measured deflection of the cantilevers produced under argon, helium, and VarigonHe30 after the supporting blocks were cut.

melt tracks and a larger fraction of lack-of-fusion pores. In addition, the narrower melt tracks resulted in an even poorer overlap of the in-fill and contour scanning (see Fig. 10b).

The identification of this subsurface porosity has important industrial implications for the post-process planning. The AM design for high-end applications, such as in aerospace, is usually combined with precision machining to improve surface roughness and remove subsurface porosity and/or other more complex processes involving, for example, abrasives and chemicals. Therefore, knowledge of the amount and spatial distribution of porosity would enable its removal, thereby improving the quality of the finished component.

4.2. Residual stresses

The subsurface residual stresses were measured on the as-built samples removed from the baseplate, allowing for more practical manipulation of samples. In addition, previous work conducted by Mishurova et al. [16] highlighted that the residual stress state of L-PBF Ti-6Al-4V cuboids still on the baseplate was similar to that of cuboids printed on support structures and removed from the baseplate.

The addition of helium to the process gas appeared to not affect the subsurface residual stresses of cuboids and plates (see Fig. 7). The reported residual stress levels are of similar magnitude as those measured on Ti-6Al-4V ELI grade 23 cuboids produced on another L-PBF system (SLM Solutions 280HL, SLM Solution Group AG) with contour scanning [16]. The stresses developed during L-PBF are limited by the material's yield strength, which, for Ti-6Al-4V, has been proven to increase with the oxygen level [7]; in the current study's case, the oxygen level was accurately monitored as below 100 ppm O_2 in all cases; consequently, no significant difference in RS was observed among the cuboid samples. This finding indicates that helium does not induce an increase in residual stress and qualifies well as an alternative process gas to produce simple samples like the plates and cuboids. These results confirm that the very fine martensitic microstructure obtained from L-PBF is responsible for the elevated yield strength of about 1000 MPa [8] and, therefore, for the RS. Several authors have demonstrated the high tensile subsurface residual stresses are compensated for by bulk compressive stresses [20,35]. Therefore, for the cuboid samples, larger stress gradients than for the plate samples were expected to appear in the subsurface regions.

Still, the study of the deflection of the cantilevers suggests that for large components of complex design, differences in residual stresses may

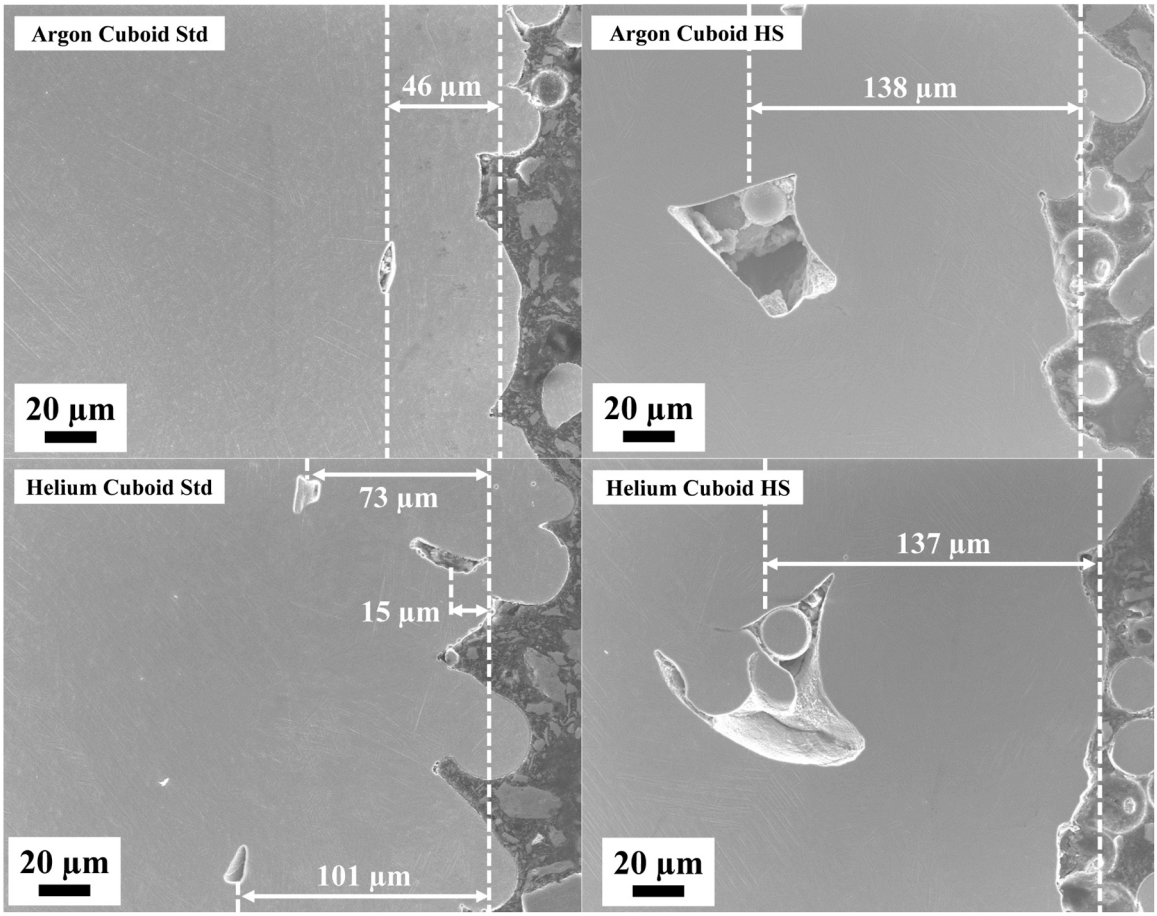

Fig. 9. Micrographs presenting subsurface porosity in the cuboids built under pure argon and helium using the standard and increased laser scanning speeds.

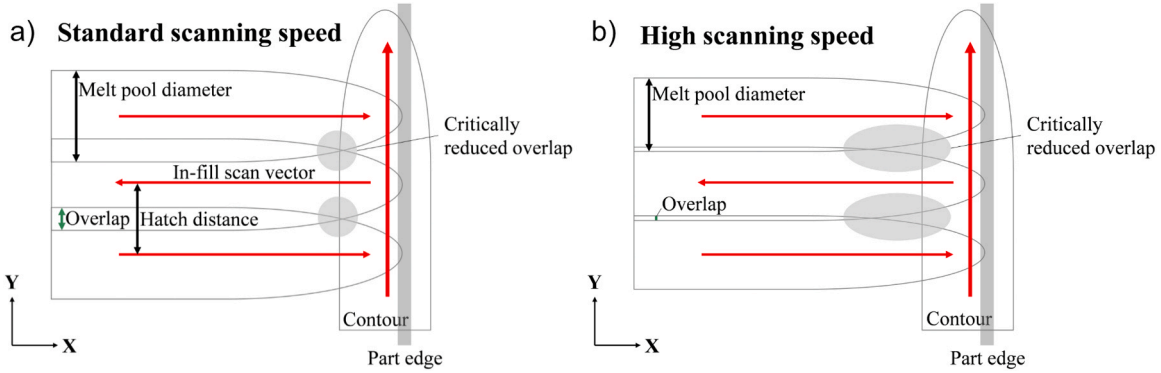

Fig. 10. Schematic representation of the melt tracks close to the part edge where the in-fill and contour tracks overlap: (a) standard scanning speed and, (b) high in-fill scanning speed.

arise from using helium (see Fig. 8). As modelled by Li et al. [31], important tensile residual stresses perpendicular to the building direction (S_{11}, in build plane) occur in the upper region of the cantilever structure while still on the baseplate and dominate the other stress components. The authors explained this result as follows. When the top layer is deposited, its expansion is limited by the material below and compressive residual stresses are obtained. Upon cooling, the contraction of this top layer is limited by the material below leading to tensile residual stresses in the upper area of the cantilever. When the supports of the cantilever are cut, the S_{11} component of the residual stress tensor becomes compressive at the top of the structure because of its plastic deformation (to conserve the equilibrium state of the residual stresses). Considering this experiment, the higher deflections under helium are connected with higher tensile stress at the top surface of the cantilever prior to the baseplate removal and could be related to higher cooling rates of this upper part because of the properties of helium. Thermocouples are not suitable due to their high response time and modern monitoring systems in L-PBF such as optical tomography and melt pool monitoring, do not allow to evaluate cooling rates. Hence, to detect such differences in cooling rates, in operando XRD, as conducted by Hocine et al. [36] at a synchrotron beamline using high speed detectors, should be used.

The characterization of the microstructures revealed no differences between samples produced with different process gases. Still, it could be that the addition of helium resulted in an enhanced heat transfer by convection at the metal-gas interface. This may have an influence for only large-scanned areas (e.g., upper part of cantilever). Without solving the heat transfer equation and deriving the heat transfer coefficient, which would require an excessive number of approximations, one can consider the following: Based on the gas properties listed in Table 3, the thermal conductivity and isobaric heat capacity of helium is evidently about 10 times higher than that of argon. In addition, the lower thermal diffusivity of argon, which is the ratio of the thermal conductivity to the volumetric heat capacity, implies a more sluggish response of argon than of helium to changes in the thermal environment.

Regardless of the process atmosphere and the scanning speed, the results highlight a significant reduction of the residual stress within the plate specimen compared to the cuboids (almost a three-fold decrease; see Fig. 7). This decrease is attributed to the heat accumulation occurring in the plate samples. The scanned XY area of the plate samples is a fifth of that of the cuboid; as a result, the scan vectors are much shorter for the plates. Hocine et al. [37] studied the effect of the length of the scan vectors on the kinetics of phase transformation occurring in Ti-6Al-4V during L-PBF, using an in-house-designed L-PBF system dedicated to synchrotron X-ray diffraction measurements. Their results highlight that the probed volume during the scanning of a layer remains in the β-phase field for short scan vectors (2 mm length) but returns to the dual-phase field for longer scan vectors (6 mm length) between each scan vector. In addition, the calculated temperatures from the recorded lattice expansion suggest that higher temperatures are retained for the smaller scanned areas and that the cooling rates are lower. The plate specimens in the current study were also produced using shorter scan vectors and thus were likely to retain higher temperatures and experience lower cooling rates than the cuboids, which is consistent with the lower measured residual stresses.

Table 3
Interesting properties of argon and helium at 500 K to consider the heat transfer problem, from Wolfram-Alpha curated data, 2020.

	Argon	Helium
Density [kg/m^3]	0.97	0.098
Thermal conductivity [W/m K]	0.027	0.23
Isobaric heat capacity [J/kg K]	520	5193
Thermal diffusivity [mm^2/s]	53	452

Relatively large areas were mapped using EBSD on the XY cross-sections of the cuboid and plate samples. Fig. 11 displays the corresponding reconstructed parent β grains, and the colour code describes the local crystallographic indexing along the building direction (Z), for the samples produced under helium. Similar maps were acquired for the samples produced with the other atmospheres, and similar conclusions were drawn. A mosaic or chess-pattern-like grain morphology was observed for this cross-section, similar to other materials processed by L-PBF, as put in evidence for 316L stainless steel by Leicht et al. [38] and Inconel® 718 by Serrano-Munoz et al. [17], while more elongated grains are typically depicted along the building direction. Thin reconstructed parent β grains are depicted around larger ones, as reported by Neikter et al. [39] under the term binary microstructure pattern, which is connected to scan vector overlaps. The normal distribution of the parent β-grain-equivalent radius of the plate sample is similar to that of the cuboid. Therefore, the heat accumulation occurring in the plate specimens is important enough to yield lower residual stresses but not to levels that would affect the grain structure. Thus, the high temperatures retained in the plate samples are likely not significantly above the β-transus temperature. Finally, the grain colouring highlights a rather weak texture regardless of sample design, with a slightly more pronounced < 001 > preferential orientation along the building direction.

Mishurova et al. [16] reported that volumetric energy density (E_V) during production has a high impact on the resulting subsurface residual stress. This impact is, however, only valid when E_V changes significantly. As shown by Mishurova et al. [16], a small decrease of E_V (by 13%) did not affect residual stress. In the present case, the usage of high-speed parameters reduced E_V by about 30% compared to the standard speed. Consistent with previous studies, no difference in residual stresses between samples produced with standard and high-speed

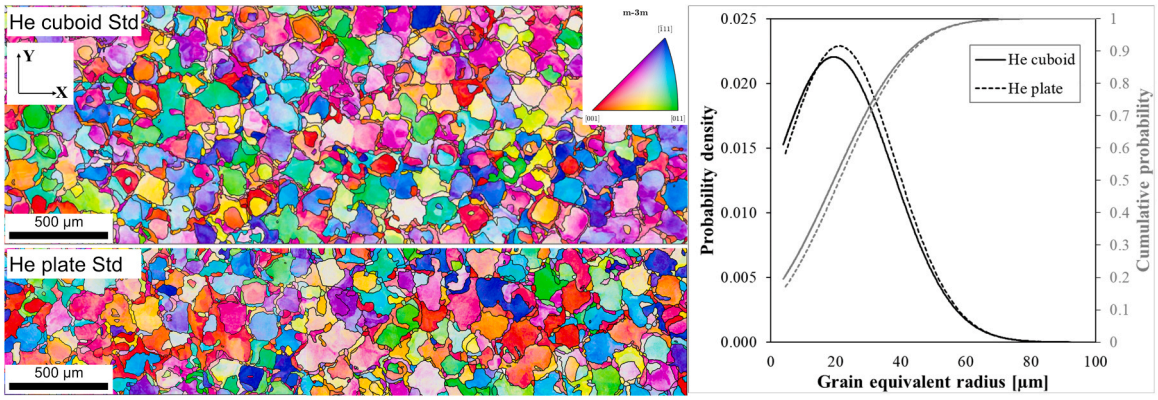

Fig. 11. Inverse pole figure maps of the reconstructed β phase with respect to the building direction for the standard helium cuboid and plate samples. The normal distribution of the grain equivalent radius of the reconstructed grains is given to the right. The grain equivalent radius is the radius of a circle with the same area as the measured grain.

parameters (see Fig. 7) was observed in the present case. It should also be emphasized that scanning strategies play a major role on the stress distribution in L-PBF produced samples. Serrano-Munoz et al. [17] put in evidence that the effect of scanning strategy on the RS distribution is closely connected to both thermal stress mechanisms and the resulting microstructure, as the results support the possible stress relaxation occurring by dislocation accumulation in case of IN718. In case of Ti-6Al-4V, Strantza et al. [40] highlighted that strategies with continuous scanning, as adopted in the present work, typically results in lower RS than strategies with shorter scan vectors, such as the so-called "island" scanning.

5. Conclusions

The measurement of the subsurface residual stresses of Ti-6Al-4V of thin plate and cuboid samples demonstrates the important effect of the component's geometry. The smaller the scan area, the lower the residual stresses, which is connected to shorter scan vectors and leads to reduced thermal gradients, without necessarily affecting the parent β-grain morphology for Ti-6Al-4V, as depicted using EBSD. The residual stresses along the building direction were reduced from a mean stress value of 645 MPa for the cuboids to 220 MPa for the plates. The increase of the laser scan speed by 40% was not reflected in changes in residual stress levels, despite the slight decrease (about 0.1%) of the density measured by laboratory XCT (the porosity volume fraction increased from 0.010% to 0.18% for the argon-produced samples). The 3D XCT reconstructions of the samples highlighted and quantified a concentration of lack-of-fusion defects at the interface between the in-fill and the contour scanning areas. This porosity volume fraction appeared larger for the helium samples; this result is likely connected to powder removal around the melt tracks, also called denudation. Still, all gases permitted to achieve high density in the bulk of the plates and cuboids. With respect to subsurface residual stress, pure helium and helium addition did not have a negative impact, even at a higher scanning speed, for which larger temperature gradients may be expected. Finally, the production of cantilevers demonstrated the effect of pure helium on the residual stress state for large and geometrically complex components. This finding supports the development of gas mixtures, such as the 30% helium addition to argon tested in this work.

The present study indicates that helium and helium additions to the gas flow have not only an interesting effect on the reduction of spatter (reported in previous work) but also an insignificant effect on the residual stresses for simple geometries. However, residual stresses can be more pronounced in more complex design features (such as cantilever samples), and further studies are necessary to guarantee the design flexibility for high-end applications.

CRediT authorship contribution statement

Pauzon: Methodology, Formal analysis, Investigation, Data curation, Writing – original draft & editing. **Mishurova:** Methodology, Formal analysis, Investigation, Data curation, Writing – original draft & editing. **Evsevleev:** Investigation, Data curation, Writing – original draft. **Dubiez-Le Goff:** Investigation, Conceptualization, Resources. **Murugesan**: Investigation, Data curation. **Bruno:** Formal analysis, Methodology, Supervision, Writing – review & editing, Project administration. **Hryha:** Conceptualization, Formal analysis, Methodology, Supervision, Writing – review & editing, Project administration.

Declaration of Competing Interest

The authors declare that they have no known competing financial interests or personal relationships that could have appeared to influence the work reported in this paper.

Acknowledgments

The work was performed in the framework of the Centre for Additive Manufacturing – Metal (CAM^2) and project Ulrica (DNr 2019–05272), supported by Vinnova. The authors would also like to acknowledge financial support from SIP LIGHTer.

The authors would like to thank Manuela Klaus and Christoph Genzel for their support during the residual stress measurements and Yiming Yao, Zhuoer Chen, and Uta Klement for their support with the EBSD map acquisition and evaluation.

References

[1] T.M. Mower, M.J. Long, Mechanical behavior of additive manufactured, powder-bed laser-fused materials, Mater. Sci. Eng. A 651 (2016) 198–213, https://doi.org/10.1016/j.msea.2015.10.068.

[2] P. Mercelis, J. Kruth, Residual stresses in selective laser sintering and selective laser melting, Rapid Prototyp. J. 12 (2006) 254–265, https://doi.org/10.1108/13552540610707013.

[3] T. Mishurova, S. Cabeza, K. Artzt, J. Haubrich, M. Klaus, C. Genzel, G. Requena, G. Bruno, An assessment of subsurface residual stress analysis in SLM Ti-6Al-4V, Materials (2017), https://doi.org/10.3390/ma10040348.

[4] A. Leicht, M. Rashidi, U. Klement, E. Hryha, Effect of process parameters on the microstructure, tensile strength and productivity of 316L parts produced by laser powder bed fusion, Mater. Charact. 159 (2020), 110016, https://doi.org/10.1016/j.matchar.2019.110016.

[5] I. Flores, N. Kretzschmar, A. Hadi, S. Chekurov, D. Bue, A. Chaudhuri, Implications of lattice structures on economics and productivity of metal powder bed fusion, Addit. Manuf. 31 (2020), 100947, https://doi.org/10.1016/j.addma.2019.100947.

[6] J. Yin, L. Yang, X. Yang, H. Zhu, D. Wang, L. Ke, Z. Wang, G. Wang, X. Zeng, High-power laser-matter interaction during laser powder bed fusion, Addit. Manuf. 29 (2019), 100778, https://doi.org/10.1016/j.addma.2019.100778.

[7] K. Dietrich J. Diller S. Dubiez-le Goff D. Bauer P. Forêt Influ. Oxyg. Chem. Compos. Mech. Prop. Ti-6Al-4V Laser Powder bed Fusion (L-PBF) 32 2020 doi: 10.1016/j.addma.2019.100980.
[8] C. Pauzon, P. Forêt, E. Hryha, T. Arunprasad, L. Nyborg, Argon-helium mixtures as laser-powder bed fusion atmospheres: towards increased build rate of Ti-6Al-4V, J. Mater. Process. Technol. 279 (2020), 116555, https://doi.org/10.1016/J.JMATPROTEC.2019.116555.
[9] C. Pauzon, P. Forêt, E. Hryha, T. Arunprasad, Effect of helium - argon mixtures as laser - powder bed fusion processing atmospheres on the properties of the built Ti-6Al-4V parts, WorldPM2018, World 2018 Bejijng (2018) 1633–1639.
[10] S. Traore, M. Schneider, I. Koutiri, F. Coste, R. Fabbro, C. Charpentier, P. Lefebvre, P. Peyre, Influence of gas atmosphere (Ar or He) on the laser powder bed fusion of a Ni-based alloy, J. Mater. Process. Technol. 288 (2021), 116851, https://doi.org/10.1016/j.jmatprotec.2020.116851.
[11] C. Pauzon, A. Leicht, U. Klement, P. Forêt, E. Hryha, Effect of the process gas and scan speed on the properties and productivity of thin 316L structures produced by laser-powder bed fusion, Metall. Mater. Trans. A. 51 (2020) 5339–5350, https://doi.org/10.1007/s11661-020-05923-w.
[12] M. Velasco-Castro, E. Hernández-Nava, I.A. Figueroa, I. Todd, R. Goodall, The effect of oxygen pickup during selective laser melting on the microstructure and mechanical properties of Ti–6Al–4V lattices, Heliyon 5 (2019) 02813, https://doi.org/10.1016/j.heliyon.2019.e02813.
[13] L. Spieß, R. Teichert, Gerd Schwarzer, H. Behnken, C. Genzel, Moderne Röntgenbeugung, Vieweg+Teubner, Wiesbaden, 2009, https://doi.org/10.1007/978-3-8349-9434-9.
[14] T. Mishurova, K. Artzt, J. Haubrich, G. Requena, G. Bruno, New aspects about the search for the most relevant parameters optimizing SLM materials, Addit. Manuf. 25 (2019) 325–334, https://doi.org/10.1016/j.addma.2018.11.023.
[15] K. Artzt, T. Mishurova, P. Bauer, J. Gussone, P. Barriobero-vila, S. Evsevleev, G. Bruno, G. Requena, J. Haubrich, Pandora's box-influence of contour parameters on roughness and subsurface residual stresses in laser powder bed fusion of Ti-6Al-4V, Materials 13 (2020) 1–24, https://doi.org/10.3390/ma13153348.
[16] T. Mishurova, K. Artzt, J. Haubrich, G. Requena, G. Bruno, Exploring the correlation between subsurface residual stresses and manufacturing parameters in laser powder bed fused ti-6al-4v, Metals 9 (2019) 261, https://doi.org/10.3390/met9020261.
[17] I. Serrano-Munoz, T. Mishurova, T. Thiede, M. Sprengel, A. Kromm, N. Nadammal, G. Nolze, R.S. Neumann, A. Evans, G. Bruno, The residual stress in as-built Laser Powder Bed Fusion IN718 alloy as a consequence of the scanning strategy induced microstructure, Sci. Rep. 10 (2020) 14645, https://doi.org/10.1038/s41598-020-71112-9.
[18] D. Apel, M. Genzel, M. Meixner, M. Boin, M. Klaus, C. Genzel, EDDIDAT: a graphical user interface for the analysis of energy- dispersive diffraction data, J. Appl. Crystallogr. 53 (2020) 1130–1137.
[19] E. Kröner, Berechnung der elastichen konstanten des vielkristalls aus den konstanten des einkristalls, Z. Phys. 151 (1958) 504–518.
[20] P. Pant, S. Proper, V. Luzin, S. Sjöström, K. Simonsson, J. Moverare, S. Hosseini, V. Pacheco, R. Lin, Mapping of residual stresses in as-built Inconel 718 fabricated by laser powder bed fusion: a neutron diffraction study of build orientation influence on residual stresses, Addit. Manuf. 36 (2020), 101501, https://doi.org/10.1016/j.addma.2020.101501.
[21] J.L. Bartlett, X. Li, An overview of residual stresses in metal powder bed fusion, Addit. Manuf. 27 (2019) 131–149, https://doi.org/10.1016/j.addma.2019.02.020.
[22] J. Schindelin, I. Arganda-carreras, E. Frise, V. Kaynig, T. Pietzsch, S. Preibisch, C. Rueden, S. Saalfeld, B. Schmid, J. Tinevez, D.J. White, V. Hartenstein, P. Tomancak, A. Cardona, Fiji - Open Source Platf. Biol. Image Anal. 9 (2019), https://doi.org/10.1038/nmeth.2019.Fiji.
[23] Thermo Fischer Scientific, Avizo Software: Thermo Fischer Scientific, (n.d.). ⟨https://www.fei.com/software/avizo⟩.
[24] A. Rack, S. Zabler, B.R. Müller, H. Riesemeier, G. Weidemann, A. Lange, J. Goebbels, M. Hentschel, W. Görner, High resolution synchrotron-based radiography and tomography using hard X-rays at the BAMline (BESSY II), Nucl. Instrum. Methods Phys. Res. Sect. A Accel. Spectrometers, Detect. Assoc. Equip. 586 (2008) 327–344, https://doi.org/10.1016/j.nima.2007.11.020.
[25] D. Paganin, S.C. Mayo, T.E. Gureyev, P.R. Miller, S.W. Wilkins, Simultaneous phase and amplitude extraction from a single defocused image of a homogeneous object, J. Microsc. Oford. 206 (2002) 33–40, https://doi.org/10.1046/j.1365-2818.2002.01010.x.
[26] T. Weitkamp, D. Haas, D. Wegrzynek, A. Rack, ANKAphase: software for single-distance phase retrieval from inline X-ray phase-contrast radiographs, J. Synchrotron Radiat. 18 (2011) 617–629, https://doi.org/10.1107/S0909049511002895.
[27] J. Yang, H. Yu, J. Yin, M. Gao, Z. Wang, X. Zeng, Formation and control of martensite in Ti-6Al-4V alloy produced by selective laser melting, Mater. Des. 108 (2016) 308–318, https://doi.org/10.1016/j.matdes.2016.06.117.
[28] S. Liu, Y.C. Shin, Additive manufacturing of Ti6Al4V alloy: a review, Mater. Des. 164 (2019), 107552, https://doi.org/10.1016/j.matdes.2018.107552.
[29] A. du Plessis, Effects of process parameters on porosity in laser powder bed fusion revealed by X-ray tomography, Addit. Manuf. 30 (2019), 100871, https://doi.org/10.1016/j.addma.2019.100871.
[30] A. du Plessis, S.G. le Roux, Standardized X-ray tomography testing of additively manufactured parts: a round robin test, Addit. Manuf. 24 (2018) 125–136, https://doi.org/10.1016/j.addma.2018.09.014.
[31] C. Li, J.F. Liu, X.Y. Fang, Y.B. Guo, Efficient predictive model of part distortion and residual stress in selective laser melting, Addit. Manuf. 17 (2017) 157–168, https://doi.org/10.1016/j.addma.2017.08.014.
[32] G.G. Stoney Tens. Met. films Depos. Electro 1909 172 175.
[33] S. Jonsson, S. Krappedal, Evaluation of residual stresses and distortions in additively manufactured components, Degree Proj. Mater. Des. Eng. (2018).
[34] P. Bidare, I. Bitharas, R.M. Ward, M.M. Attallah, A.J. Moore, Laser powder bed fusion in high-pressure atmospheres, Int. J. Adv. Manuf. Technol. 99 (2018) 543–555, https://doi.org/10.1007/s00170-018-2495-7.
[35] B. Ahmad, S.O. Van Der Veen, M.E. Fitzpatrick, H. Guo, Residual stress evaluation in selective-laser-melting additively manufactured titanium (Ti-6Al-4V) and inconel 718 using the contour method and numerical simulation, Addit. Manuf. 22 (2018) 571–582, https://doi.org/10.1016/j.addma.2018.06.002.
[36] S. Hocine, H. Van Swygenhoven, S. Van Petegem, C. Sin, T. Chang, T. Maimaitiyili, G. Tinti, D.F. Sanchez, D. Grolimund, N. Casati, Operando X-ray diffraction during laser 3D printing, Mater. Today 34 (2020) 30–40, https://doi.org/10.1016/j.mattod.2019.10.001.
[37] S. Hocine, H. Van Swygenhoven, S. Van Petegem, C. Sin Ting Chang, T. Maimaitiyili, G. Tinti, D. Ferreira Sanchez, D. Grolimund, N. Casati, In operando X-ray diffraction during laser 3D printing, Mater. Today (2019) 1–12, https://doi.org/10.1016/j.mattod.2019.10.001.
[38] A. Leicht, C.H. Yu, V. Luzin, U. Klement, E. Hryha, Effect of scan rotation on the microstructure development and mechanical properties of 316L parts produced by laser powder bed fusion, Mater. Charact. 163 (2020) 2–10, https://doi.org/10.1016/j.matchar.2020.110309.
[39] M. Neikter, A. Huang, X. Wu, Microstructural characterization of binary microstructure pattern in selective laser-melted Ti-6Al-4V, Int. J. Adv. Manuf. Technol. 104 (2019) 1381–1391, https://doi.org/10.1007/s00170-019-04002-8.
[40] M. Strantza, R.K. Ganeriwala, B. Clausen, T.Q. Phan, L.E. Levine, D.C. Pagan, J. Ruff, W.E. King, N.S. Johnson, R.M. Martinez, V. Anghel, G. Rafailov, D. W. Brown, Effect of the scanning strategy on the formation of residual stresses in additively manufactured Ti-6Al-4V, Addit. Manuf. 45 (2021), 102003, https://doi.org/10.1016/j.addma.2021.102003.